Journal of the Taiwan Institute of Chemical Engineers 93 (2018) 315–328

Contents lists available at ScienceDirect

Journal of the Taiwan Institute of Chemical Engineers

journal homepage: www.elsevier.com/locate/jtice

Perovskite-like photocatalyst, $PbBiO_2Br/PbO/g\text{-}C_3N_4$: Synthesis, characterization, and visible-light-driven photocatalytic activity

Yi-Chuen Wang, Ai-Hsuan Lee, Chiing-Chang Chen*

Department of Science Education and Application, National Taichung University of Education, Taichung 403, Taiwan

ARTICLE INFO

Article history:
Received 9 May 2018
Revised 18 July 2018
Accepted 26 July 2018
Available online 28 August 2018

Keywords:
$PbBiO_2Br$
PbO
$g\text{-}C_3N_4$
Composites
Photocatalytic

ABSTRACT

Lead bismuth oxybromide ($PbBiO_2Br$) is a powerful perovskite-like semiconductor that can be used with visible light. $PbBiO_2Br$ is a perovskite-like photocatalyst that has recently received scholarly attention. Until now, scholars have not published studies regarding $PbBiO_2Br/PbO/g\text{-}C_3N_4$-mediated crystal violet (CV) dye and 2-Hydroxybenzoic Acid (HBA) photodegradation under irradiation with visible light. The current paper reports the first composite isolation of $PbBiO_2Br/PbO/g\text{-}C_3N_4$; characterization was realized through XRD, TEM, FE-SEM-EDS, HR-XPS, FI-IR, PL, BET, and UV-DRS. Photocatalytic efficiency observation proved that using $PbBiO_2Br/PbO/g\text{-}C_3N_4$ produced the highest observed reaction rate, namely 0.1981 h^{-1}. This derivation exceeded the derivations for the $PbBiO_2Br$, PbO, $g\text{-}C_3N_4$ photocatalysts, and $PbBiO_2Br/PbO$ by 1.23, 34.2, 4.3, and 1.2 times, respectively. Four scavengers demonstrated quenching effects. The $O_2^{\bullet-}$ radical was critical to HBA degradation, whereas the $^{\bullet}OH$ radical and $^1O_2$ species played minor roles in the observed CV dye degradation. The present paper proposes and explains possible photocatalytic degradation mechanisms. This study's methods of $PbBiO_2Br/PbO/g\text{-}C_3N_4$ synthesis and photocatalytic degradation of CV can be useful for future treatment of wastewater.

1. Introduction

In the 21st century, numerous societies worldwide have faced increasing challenges related to water. Each population seeks reliable access to safe water and convenient disposal of wastewater that does not threaten the environment or harm water resources. All countries are facing increasingly daunting problems of environmental pollution and energy demands; photocatalysis is not only sufficient for solar energy conversion but also for pollutant degradation [1]; therefore photocatalysis can address the challenges of water supply. A low-cost, environmentally friendly photocatalyst is critical for practical photocatalysis [2].

Scholars have broadly explored the structures of compounds that are based on bismuth, are layered, and are part of the Aurivillius family—which includes BiOX (X = Cl, Br, I) [3-6], $Bi_4Ti_3O_{12}$ [7], and $BiVO_4$ [8]—for use as highly efficient photocatalysts; this is because such compounds exhibit distinct layered structures and high catalytic efficiency. The levels of Bi 6s and O 2p are considered to cause a hybridized valence band (VB) that is preponderantly dispersed; this property advances photoformed-hole mobility and oxidation reactions, consequently inducing photoformed electron–hole pair separation and subsequent photocatalytic activity improvement [9]. The structures of numerous inorganic compounds have been determined to contain relevant components, with different functions supervised by individual units. $[Bi_2O_2]^{2+}$ slabs that exhibit an α-PbO-type structure, in addition to having simple halide layers, constitute effective spacers in certain functional materials that are layered [10]. Studies on the mechanisms associated with the diverse photocatalytic activities of layered lead bismuth oxyhalide ($PbBiO_2X$)-type materials (X = Cl, Br, I) have mainly discussed electronic topics [11-18]. However, any clarification of the photocatalytic properties of the materials should also consider crystal-chemical contentions. These metal oxides' crystal structures, optical properties, and redox properties might collectively explain their divergent catalytic activities. A common property among all the discussed solid compounds is related to their crystallization in layered structures. The compounds have halide-layer-separated covalent bi-metal oxygen layers $[PbBiO_2]^+$ stacked along the [001] direction. One can assume that the crystal surface is composed of layers of bimetallic oxygen; one expects that the (001) surfaces would be made up of atoms from two types of metals. Statistics have proven that lead and bismuth reside in the metal positions at a 1:1 ratio [19]. The band gap values of $PbBiO_2I$ [20,21], $PbBiO_2Br$ [11,22-24], and $PbBiO_2Cl$ [12] are 2.39, 2.47, and 2.53 eV, respectively. These values indicate that the gaps determined for all the aforementioned semiconductors exist in the visible-light region; hence, they can be applied in photocatalysis.

* Corresponding author.
E-mail address: ccchen@mail.ntcu.edu.tw (C.-C. Chen).

https://doi.org/10.1016/j.jtice.2018.07.037
1876-1070/

Studies have reported that heterojunctions associated with $PbBiO_2X$—which include $PbBiO_2Br$/BiOBr [11], $PbBiO_2Br$/g-C_3N_4 [25], $PbBiO_2Br$/UiO-66-NH_2 [26], AgBr/Ag/$PbBiO_2Br$ [27], $PbBiO_2Br$/$NbSe_2$ [28], $PbBiO_2Cl$/BiOCl [13], $PbBiO_2I$/PbO [29], and MoS_2/$PbBiO_2I$ [30]—exhibit improved photocatalytic activity. Therefore, an ion exchange reaction that partly transforms $PbBiO_2Br$ into $NbSe_2$ through a direction that is thermodynamically favored is feasible; such a partial transformation would enable the component ions to connect in exchange processes with incoming species [31], consequently producing a $PbBiO_2Br$/$NbSe_2$ heterojunction.

We observed, after a survey of the pertinent literature, that $PbBiO_2Br$/PbO/g-C_3N_4 –containing nanocomposite semiconductors have yet to be reported. The current study presents the first known synthesis of $PbBiO_2Br$/PbO/g-C_3N_4 nanocomposites through a template-free hydrothermal method. Crystal violet (CV) degradation was demonstrated in aqueous solution under visible light irradiation; the corresponding photocatalytic efficiencies of several prepared $PbBiO_2Br$/PbO/g-C_3N_4 composites were explored.

2. Experimental details

2.1. Materials

Merck supplied isopropanol (IPA), CH_3COONH_4 (reagent grade), NaOH, HNO_3, and methanol (high-performance liquid chromatography (HPLC) grade). Other vendors supplied $Bi(NO_3)_3$•$5H_2O$ (Katayama), KBr (Katayama), $Pb(NO_3)_2$•H_2O (Osaka), CV dye (TCI), 2-hydroxybenzoic acid (HBA; salicylic acid), sodium azide (SA, Sigma-Aldrich), ammonium oxalate (AO, Osaka), and *p*-benzoquinone (BQ, Alfa Aesar), all of which were used as obtained.

2.2. Analytical instruments and methods

A microscope (JEOL-2010; 200-kV acceleration voltage) was employed in this study for executing field-emission transmission electron microscopy (FE-TEM), selected-area electron diffraction, high-resolution transmission electron microscopy (HR-TEM), and energy-dispersive spectroscopy (EDS). Furthermore, a JEOL JSM-7401F device (15-kV acceleration voltage) was employed in this study for field-emission scanning electron microscopy (FE-SEM)-EDS. A MAC Science MXP18 apparatus was operated at 40 kV with Cu-Kα radiation. X-ray diffraction (XRD) was executed at 80 mA. Additionally, 15-kV Al-Kα radiation was utilized. The samples' Brunauer–Emmett–Teller (BET) specific surface areas (S_{BET}) were measured with a Micrometrics Gemini automated system; the adsorbate was nitrogen gas that was at the temperature of liquid nitrogen. High-resolution X-ray photoelectron spectroscopy (HR-XPS) and ultraviolet photoelectron spectroscopy were conducted with an ULVAC-PHI XPS (PHI Quantera SXM).

Separation and identification processes were completed using a liquid chromatography/mass spectrometry (LC/MS) apparatus (Waters ZQ) comprising an auto-sampler, binary pump, micromass detector, and photodiode-array-detector. The residual dye amount for each reaction cycle was quantified with HPLC-MS. After chromatographic conditions had been readjusted to ensure the compatibility of the mobile phase, organic intermediates were analyzed with HPLC-MS (Solvent A: aqueous ammonium acetate buffer (25 mM, pH 6.9); Solvent B: methanol). HPLC was conducted with an Atlantis^{TM} dC18 column (250 mm × 4.6 mm, i.d.; 5 µm, dp, 1.0 mL/min mobile flow rate). The linear gradient was: $t = 0$, $A = 95$, $B = 5$; $t = 20$, $A = 50$, $B = 50$; $t = 35$–40, $A = 10$, $B = 90$; $t = 45$, $A = 95$, $B = 5$. The column's product was added to the mass spectrometer's electrospray ionization source [32].

2.3. Synthesis of $PbBiO_2Br$/PbO and g-C_3N_4

In a 50-mL flask, $Pb(NO_3)_2$•H_2O (1, 3, and 5 mmol) and $Bi(NO_3)_3$•$5H_2O$ (3 mmol) were combined; then 15 mL of 1 M HNO_3 was added. Next, 5 M NaOH was added in drops under continuous stirring to adjust the pH within 1–7. After a white precipitate had formed, 1 mL of 1 M KBr was also dropped in. The solution was stirred vigorously for 30 min, after which 24 mL was transferred to an autoclave (30 mL) that was lined with Teflon; the autoclave was heated to 100–150 °C for 12 h, and then allowed to cool to room temperature. A solid precipitate was gathered in a filter; the derived precipitate was washed with deionized water and ethanol to purge any ionic species; the precipitate was dried at 60 °C overnight. Composites of $PbBiO_2Br$/PbO were realized using the relevant $Bi(NO_3)_3$•$5H_2O$/$Pb(NO_3)_2$•H_2O molar ratio (3:1, 3:3, or 5:3), pH value, temperature, and reaction time (12 h); for the as-prepared samples labeled as shown in Table 1, the formulated designations ranged from B3P1B1-1-100 to B3P5B1-4-150.

2.4. Synthesis of g-C_3N_4

We synthesized g-C_3N_4 powder under atmospheric conditions. We directly calcinated melamine in a muffle furnace. Various procedures can produce this powder. In our process, we placed 5 g of melamine in a semiclosed alumina crucible with a cover. We heated the crucible to 520 °C for 4 h (heating rate: 10 °C/min). After the derived product had cooled to room temperature, we obtained g-C_3N_4 powder.

2.5. Synthesis of $PbBiO_2Br$/PbO/g-C_3N_4

This process entailed first mixing $PbBiO_2Br$/PbO (500–x mg) and g-C_3N_4 (x mg) in a 50-mL flask and then introducing ethylene glycerol (10 mL). For the as-prepared samples, the formulated designations ranged from B3P1B1-1-100-1wt% to B3P5B1-4-150-50wt% (labeled as shown in Table 1). We stirred the material vigorously for 30 min; 30 mL was transferred to a Teflon-lined autoclave (30 mL). The autoclave was heated to 100–150 °C for 12 h, and then allowed to cool to room temperature. The derived solid precipitate was filtered and then washed with deionized water and ethanol to remove any ionic species. Then, the precipitate was dried at 60 °C overnight.

2.6. Photocatalytic experiments

An aqueous solution of CV dye was stirred, transferred to a 100-mL flask, and irradiated. After the aqueous CV suspension (100 mL, 10 ppm) had been mixed with 10 mg of catalyst powder, the mixture was put in a Pyrex flask. The pH of the mixture was regulated by adding solutions containing NaOH or HNO_3. We conducted procedures in darkness for accurate measurement of the adsorption–desorption equilibrium. An orbital shaker (100 rpm) continually agitated the mixture; its temperature was held constant. The mixture was stirred with a magnetic stirring device for 30 min in darkness; this ensured equilibrium of adsorption and desorption between the CV mixture and the catalyst surface. Irradiation was supplied by Xe arc lamps (10 W) positioned 30 cm from the sample; a 400-nm cut-off filter was present; the light shone at 2.7 W/m^2. We collected a 5-mL aliquot and centrifuged the catalyst from it. We used HPLC-PDA-MS to quantify the residual dye for each reaction cycle.

2.7. Quenching experiments

We applied four quenchers to measure the effects of active species on the photocatalytic reaction. These quenchers scavenged some active species. Four active species, namely $^{\bullet}OH$, $O_2^{\bullet-}$, h^+,

Table 1
Codes of as-prepared samples under different hydrothermal conditions.

Molar ratio (Bi: Pb) = 3:1					
Temp (°C)/pH	g-C_3N_4 wt (%)				
	1	5	10	25	50
150-7	B3P1B1-7-150-1wt%	B3P1B1-7-150-5wt%	B3P1B1-7-150-10wt%	B3P1B1-7-150-25wt%	B3P1B1-7-150-50wt%
150-4	B3P1B1-4-150-1wt%	B3P1B1-4-150-5wt%	B3P1B1-4-150-10wt%	B3P1B1-4-150-25wt%	B3P1B1-4-150-50wt%
Molar ratio (Bi: Pb) = 3:3					
Temp (°C)/pH	g-C_3N_4 wt (%)				
	1	5	10	25	50
150-4	B3P3B1-4-150-1wt%	B3P3B1-4-150-5wt%	B3P3B1-4-150-10wt%	B3P3B1-4-150-25wt%	B3P3B1-4-150-50wt%
100-1	B3P3B1-1-100-1wt%	B3P3B1–1-100-5wt%	B3P3B1-1-100-10wt%	B3P3B1-1-100-25wt%	B3P3B1-1-100-50wt%
Molar ratio (Pb: Bi) = 3:5					
Temp (°C)/pH	g-C_3N_4 wt (%)				
	1	5	10	25	50
150-4	B3P5B1-4-150-1wt%	B3P5B1-4-150-5wt%	B3P5B1-4-150-10wt%	B3P5B1-4-150-25wt%	B3P5B1-4-150-50wt%
100-1	B3P5B1-1-100-1wt%	B3P5B1-1-100-5wt%	B3P5B1-1-100-10wt%	B3P5B1-1-100-25wt%	B3P5B1-1-100-50wt%

Table 2
Crystalline phase changes of as-prepared samples under different bismuth oxyiodide weight of g-C_3N_4. (♦ $PbBiO_2Br$ ● BiOBr □PbO ♥ Pb_2O_3 ▣ g-C_3N_4 ■ Bi_3O_4Br).

Molar ratio (Bi : Pb) = 3:1					
Temp (°C)/	g-C_3N_4 weight (%)				
pH	1	5	10	25	50
150-7	♦□▣	♦□▣	♦□▣	♦□▣	♦□▣
150-4	♦●□▣	♦●□▣	♦●□▣	●♥▣	●♥▣
Molar ratio (Bi : Pb) = 3:3					
Temp (°C)/	g-C_3N_4 weight (%)				
pH	1	5	10	25	50
150-4	♦●□♥▣	♦●□♥▣	♦●□♥▣	♦●□♥▣	♦●□♥▣
100-1	●■▣	●▣	●▣	●▣	●▣
Molar ratio(Bi : Pb)= 3:5					
Temp (°C)/	g-C_3N_4 weight (%)				
pH	1	5	10	25	50
150-4	♦●□♥▣	♦●□♥▣	♦●□♥▣	♦●□♥▣	♦●□♥▣
100-1	●■▣	●▣	●▣	●▣	●▣

and $^1O_2$, were scavenged by IPA (1.0 mM) [33]; BQ (1.0 mM) [34]; AO (1.0 mM) [35]; and SA (1.0 mM) [36] respectively.

3. Results and discussion

3.1. Characterization of as-prepared samples

3.1.1. XRD

Fig. S1 of the supplementary data depicts the XRD patterns of the as-prepared samples; the patterns clearly indicate the existence of the composites $PbBiO_2Br$/PbO, $PbBiO_2Br$/PbO/BiOBr, Bi_3O_4Br/BiOBr, $PbBiO_2Br$/PbO/Pb_2O_3/BiOBr, $PbBiO_2Br$/PbO/Pb_2O_3, $PbBiO_2Br$/Bi_2O_3, and $PbBiO_2Br$/Pb_2O_3/Bi_2O_3. Table S1 summarizes the results of the XRD measurements. All the as-prepared samples contain $PbBiO_2Br$ (JCPDS 38-1008), BiOBr (JCPDS 78-0348), Bi_3O_4Br (JCPDS 84-0793), PbO (JCPDS 085-1287), Bi_2O_3 (JCPDS 71-0465), and Pb_2O_3 (JCPDS 036-0725). In these experiments, pH played a key role, and temperature and molar ratio played minor roles in controlling the composition and anisotropic growth of crystals. From the results of Table S1, the controlled morphology and crystal phase of $PbBiO_2Br$/PbO could be completed by simply changing some reaction parameters, including temperature and pH value.

Fig. 1 and Fig. S2 illustrate the as-prepared samples' XRD patterns, clearly demonstrating the following composites' existence: $PbBiO_2Br$/PbO/g-C_3N_4, $PbBiO_2Br$/PbO/BiOBr/g-C_3N_4, Pb_2O_3/BiOBr/g-C_3N_4, $PbBiO_2Br$/Pb_2O_3/BiOBr/g-C_3N_4, Bi_3O_4Br/BiOBr/g-C_3N_4, and

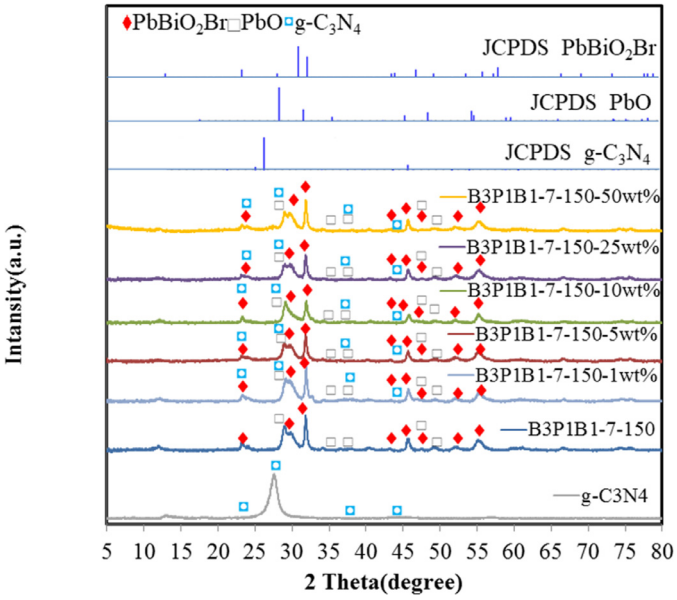

Fig. 1. XRD patterns of the as-prepared samples obtained by using different content of g-C3N4, at reaction temperature 150 °C and reaction times 12 h. (Molar ratio $Bi(NO_3)_3/Pb(NO_3)_2 = 3/1$).

BiOBr/g-C_3N_4. The results revealed that the as-prepared samples had the following phases: $PbBiO_2Br$ (JCPDS 38-1008), BiOBr (JCPDS 78-0348), Bi_3O_4Br (JCPDS 84-0793), PbO (JCPDS 085-1287), Pb_2O_3 (JCPDS 036-0725), and g-C_3N_4 (JCPDS 87-1526). Scholars have recognized that a hydrothermal reaction's molar ratio and pH value considerably influence the products' compositions and morphologies. Scholars who have completed controlled experiments aimed at probing the influence of molar ratio and pH on such a reaction have reported pH and molar ratio to be integral in controlling crystal composition and anisotropic growth, but temperature is not essential [32,37]. $PbBiO_2Br$/PbO/g-C_3N_4 was derived at a pH of 7, a molar ratio (Bi/Pb) of 3/1, and a reaction temperature of 150 °C. Table 1 provides a summary of the acquired XRD results in this study.

3.1.2. TEM

Fig. 2 illustrates the variously sized layers of $PbBiO_2Br$/PbO/g-C_3N_4 (B3P1Br-150-7-12-1wt%); this is in agreement with the TEM observations. As demonstrated by the HR-TEM image that is depicted in Fig. 2(c), three sets of lattice images revealed D-spacing values of 0.641, 0.212, and 0.320 nm; these were attributed to the (002), (102), and (110) planes of $PbBiO_2Br$, PbO, and g-C_3N_4, respectively; this observation agreed with the XRD results. In Fig. 2(d), Bi, Pb, Br, O, C, and N were also determined to be the constituents of the derived sample, as indicated by the EDS spectrum. The results suggest that the $PbBiO_2Br$/PbO/g-C_3N_4 phase construction promoted photoinduced carrier segregation, and engendered high levels of photocatalytic activity.

3.1.3. Morphological structure and composition

Fig. 3 and Fig. S4 depict the $PbBiO_2Br$/PbO/g-C_3N_4 FE-SEM images; the images derived are depicted at a high level of magnification. The $PbBiO_2Br$, PbO, and g-C_3N_4 samples' morphologies were noted to resemble an irregular plate, long rod, and irregular nanosheet. The SEM-EDS results demonstrated that the samples mostly consisted of Pb, Bi, O, Br, C, and N (Table 3 and Table S2). The Pb Bi^{-1} atomic ratios of the lead bismuth oxybromides samples were within the range of 0–1.02, which corresponded to pure phase BiOBr, $PbBiO_2Br$/BiOBr, $PbBiO_2Br$, and $PbBiO_2Br$/PbO, compared to the stoichiometric ratio (Pb: Bi = 0, 0.5, 1 and 2), and could be selectively synthesized through a hydrothermal method. The possible processes for the synthesis of lead bismuth oxybromides were described as Eqs. (1)–(13). The Pb N^{-1} atomic ratios of the $PbBiO_2Br$/PbO/g-C_3N_4 composites were within the range of 0–0.23, which corresponded to pure phase g-C_3N_4, PbO/g-C_3N_4, $PbBiO_2Br$/g-C_3N_4, $PbBiO_2Br$/BiOBr/g-C_3N_4, and $PbBiO_2Br$/PbO/g-C_3N_4, compared to the stoichiometric ratio (Pb:N = 0, 0.25, 0.25, and 0.5), and could be selectively synthesized through a hydrothermal method. The possible processes for the synthesis of $PbBiO_2Br$/PbO/g-C_3N_4 composites were described as Eqs. (1)–(15). From above results, a series of $PbBiO_2Br$/PbO/g-C_3N_4 composites could be selectively synthesized through a controlled hydrothermal method. The aforementioned results reveal the controlled hydrothermal method to be effective for realizing selective composite synthesis. Fig. S3 depicts the FE-SEM images of the as-prepared samples; the images derived are depicted at a high level of magnification. The samples' morphologies were noted to resemble an irregular nanosheet, irregular plate, particle, long rod, and cube. The SEM-EDS results demonstrated that the samples mostly consisted of Pb, Bi, O, Br, C, and N (Table S2). The aforementioned results reveal the controlled hydrothermal method to be effective for realizing selective composite synthesis.

Table 3
EDS of the as-prepared $PbBiO_2Br$/PbO materials obtained by using different content of g-C_3N_4, at reaction temperature 150 °C and reaction times 12 h. (Molar ratio $Bi(NO_3)_3/Pb(NO_3)_2 = 3/1;3/3;3/5$).

Sample code	EDS of atomic ratio (%)					
	Pb	Bi	O	Br	C	N
B3P1B1-7-150-12	5.48	20.64	64.87	9.02	–	–
1 wt%	0.60	2.82	15.77	0.44	52.92	27.46
5 wt%	0.65	7.21	20.67	1.91	41.52	28.05
10 wt%	2.57	11.65	43.85	3.36	27.62	10.96
25 wt%	1.03	10.25	32.13	3.28	35.05	18.26
50 wt%	0.74	2.32	12.92	0.66	44.49	38.87
B3P1B1-4-150-12	6.06	23.59	63.87	6.47	–	–
1 wt%	0.69	3.22	20.87	1.12	28.55	45.55
5 wt%	0.44	2.94	9.19	0.79	48.00	38.65
10 wt%	0.32	2.01	12.05	0.78	48.19	36.65
25 wt%	0.00	1.93	11.38	1.06	39.72	45.92
50 wt%	0.36	2.55	8.81	0.61	29.87	57.80
B3P3B1-4-150-12	9.03	14.43	73.38	4.19	–	–
1 wt%	0.50	3.53	23.85	0.85	28.61	42.67
5 wt%	0.49	0.89	9.29	0.18	43.86	45.28
10 wt%	0.61	1.34	12.06	0.52	42.38	43.09
25 wt%	0.21	0.62	6.17	0.18	41.87	50.96
50 wt%	3.04	8.17	32.44	2.48	10.84	43.04
B3P3B1-1-100-12	–	28.29	66.05	5.67	–	–
1 wt%	–	8.87	27.29	5.58	15.49	42.77
5 wt%	–	16.29	51.19	2.33	11.27	18.91
10 wt%	–	16.72	52.26	1.07	16.29	13.66
25 wt%	–	16.71	36.36	6.03	13.16	27.75
50 wt%	–	5.2	12.86	1.56	33.45	46.93
B3P5B1-4-150-12	9.36	19.18	63.99	7.46	–	–
1 wt%	2.76	12.32	45.09	3.83	9.90	26.09
5 wt%	0.69	1.15	17.78	0.49	24.80	55.09
10 wt%	2.82	10.62	39.25	3.86	9.02	34.43
25 wt%	2.41	11.93	36.31	3.19	14.10	32.05
50 wt%	1.34	2.50	13.59	0.70	29.79	52.07
B3P5B1-1-100-12	–	29.87	53.65	16.48	–	–
1 wt%	–	3.05	13.93	1.27	37.46	44.30
5 wt%	–	7.27	18.50	5.96	26.69	41.58
10 wt%	–	5.58	29.79	2.01	20.68	41.94
25 wt%	–	2.08	11.56	1.07	35.99	49.30
50 wt%	–	0.79	4.74	0.39	55.93	38.15

3.1.4. Fourier-transform infrared spectroscopy

Fig. 4 presents the $PbBiO_2Br$/PbO/g-C_3N_4 composites' Fourier-transform infrared spectroscopy spectra (realized at various weight

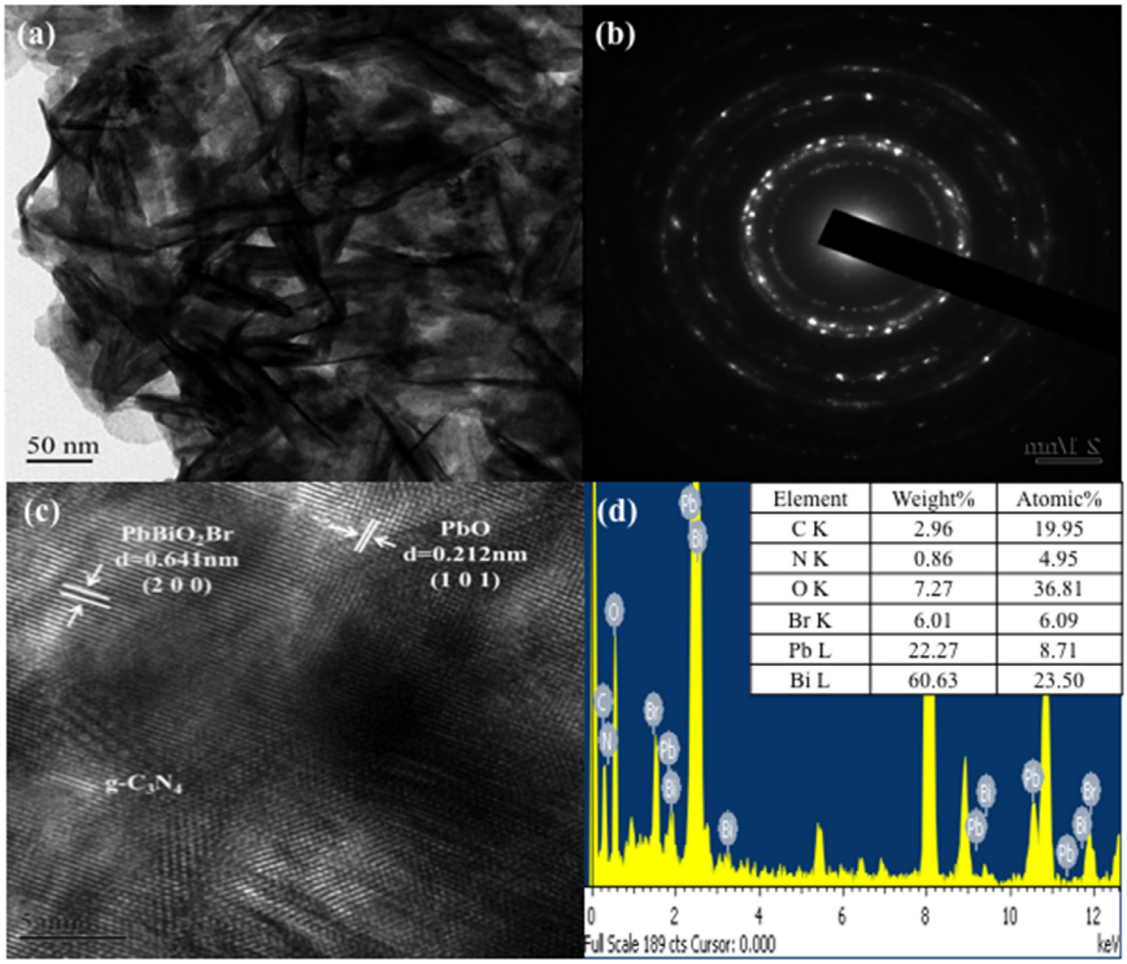

Fig. 2. (a) FE-TEM images, (b) SAD, (c) HR-TEM, and (d) EDS of $PbBiO_2Br/PbO/g\text{-}C_3N_4$ (B3P1B1-150-7-12-1wt%) sample by the hydrothermal autoclave method.

percentages). These spectra reveal a strong absorption located mainly at 400–900 cm^{-1}; this was noted in this study to correspond to Bi–O, Bi–O–Br, Bi–O–Bi, and Pb–O in $PbBiO_2Br/PbO$ stretching vibrations [38]. Concerning pure $g\text{-}C_3N_4$, peaks were observed at 1253, 1327, 1421, 1573, and 1640 cm^{-1}, noted in this study to correspond to the typical stretching modes that are associated with the CN heterocycles [39,40]. Additionally, the results revealed the breathing mode typical to the triazine units to be located at 812 cm^{-1} [41]; this agreed with the XRD- and TEM-derived results. Furthermore, ν(C–O) stretching vibrations were noted to be represented by a strong broad band that was located at 1381 cm^{-1}. The (OCO) out-of-plane vibration was indicated to be represented by a moderately strong band that was located at approximately 820 cm^{-1}. This was manifested by the $PbCO_3$ infrared spectra.

3.1.5. XPS

Fig. 5 presents the $PbBiO_2Br/PbO/g\text{-}C_3N_4$ composites' Bi 4f, Br 3d, C 1s, N 1s, O 1s, and Pb 4f XPS spectra, with the transition peaks associated with the orbitals of Bi 4f, Br 3d, C 1s, N 1s, O 1s, and Pb 4f indicating Bi, Br, C, N, O, and Pb to be the constituents of the derived catalysts. Fig. 5(b) reveals the spectra derived for Bi 4f to have two peaks at 158.7- and 164.3-eV binding energies ascribed to Bi $4f_{7/2}$ and $4f_{5/2}$, which were also determined to be attributable to Bi existing in a trivalent oxidation state. The Bi^{3+} phases within the $PbBiO_2Br/PbO/g\text{-}C_3N_4$ composites can explain these $4f_{7/2}$ peaks. Chen et al. [42] also indicated a comparable chemical binding observation for Bi 4f. The peaks observed at 67.9- and 69.0-eV binding energies, as shown in Fig. 5(c), were determined to correspond to Br $3d_{5/2}$ and $3d_{3/2}$, and this was ascribed to Br existing in the monovalent oxidation state for $PbBiO_2Br$. Fig. 5(d) illustrates the composites' HR C 1s spectra, demonstrating primarily two carbon species: sp^2 C–C bonds (284.6 eV), sp^2-hybridized carbon that was determined to exist in the aromatic ring containing N (N–C=N) (285.8 eV) and sp^2-hybridized carbon that was determined to exist in the aromatic ring containing O (N–C=O) (288.6 eV). A study demonstrated O (N–C=O) to be the primary species in polymeric $g\text{-}C_3N_4$ [43]. As illustrated in Fig. 5(e), the spectra of N1s could be deconvoluted into three peaks at 397.9, 398.6, and 399.9 eV. The highest peak that was centered at 398.6 eV was determined to correspond to sp^2-hybridized N contained in triazine rings (C–N=C), and that noted at 397.9 eV was determined to correspond to the tertiary $N\text{–}(C)_3$ groups. Both units, in addition to sp^2-hybridized carbon (N–C=N, 285.8 eV), were determined to constitute the units of heptazine heterocyclic rings, thus forming the fundamental units of the substructure of $g\text{-}C_3N_4$ polymers. Finally, the weak peak that was observed at 399.9 eV was determined to correspond to the effects of charging or to positive charge localization in heterocycles [44]. Furthermore, the asymmetric peak derived from the O 1 s spectra shown in Fig. 5(f) could be decomposed using a program for XPS peak fitting, yielding three O 1 s peaks at 529.5, 530.9, and 532.0 eV, which were determined to correspond to $PbBiO_2Br$ and PbO lattice oxygen atoms and M–OH [32]. Fig. 5(g) indicates the spectra derived for Pb 4f to be deconvoluted into peaks at 137.4- and 138.1-eV binding energies, ascribed to Pb $4f_{7/2}$, which

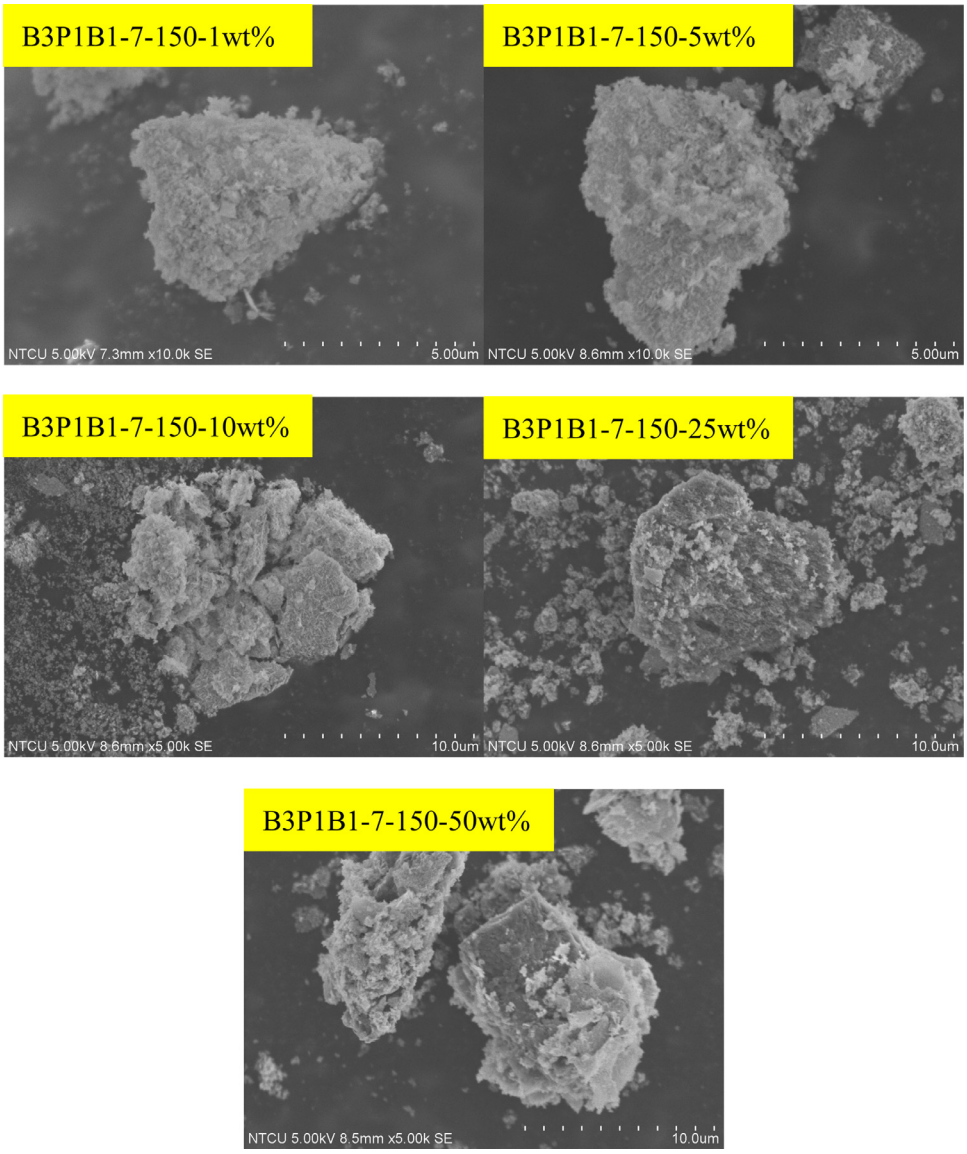

Fig. 3. SEM images of as-prepared samples obtained by using different content of g-C3N4. (Molar ratio $Bi(NO_3)_3/Pb(NO_3)_2 = 3/1$, pH = 7, reaction temp = 150 °C, reaction time = 12 h).

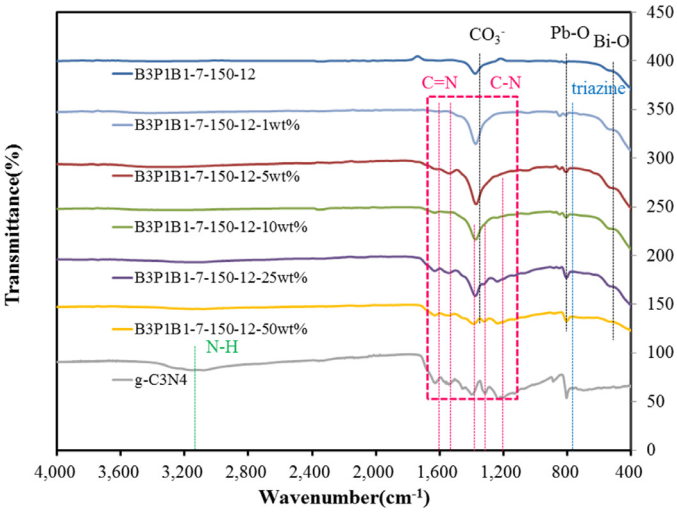

Fig. 4. FT-IR spectra of as-prepared samples with various levels of g-C3N4. (Molar ratio $Bi(NO_3)_3/Pb(NO_3)_2 = 3/1$, pH = 7, reaction temp = 150 °C, reaction time = 12 h).

could be attributed to Pb existing in a divalent oxidation state [45]. Chen et al. reported that $PbBiO_2Cl$ and PbO particle sizes might be correlated with discernible variations in the Pb peak binding energy; furthermore, they reported that the peak's relative integral intensity depended on a particle fraction in some specific region [13,29,46]; this indicated that greater successive ionic layer adsorption and reaction cycles produced large particles and small particles on the surfaces of titania nanotubes. We observed a pair of Pb^{2+} phases; we attributed the first to the 137.4 eV $4f_{7/2}$ peak and the second to the 138.1 eV $4f_{7/2}$ peak. The presented results were concordant with the XRD and TEM results.

Chen et al. [13,42,47,48] have demonstrated formation processes associated with a sequence of bismuth oxybromides and lead bismuth oxychlorides. Eqs. (1)–(12) describe the $PbBiO_2Br/PbO$ formation processes proposed by the current study. The compounds that were realized under various hydrothermal conditions were demonstrated to undergo a series of changes, described as $BiOBr \rightarrow Bi_4O_5Br_2 \rightarrow Bi_{24}O_{31}Br_{10} \rightarrow Bi_3O_4Br \rightarrow Bi_5O_7Br \rightarrow \alpha\text{-}Bi_2O_3$, $PbBr_2 \rightarrow Pb(OH)Br \rightarrow PbBiO_2Br$, $Pb(OH)_2 + BiOBr \rightarrow PbBiO_2Br$, and

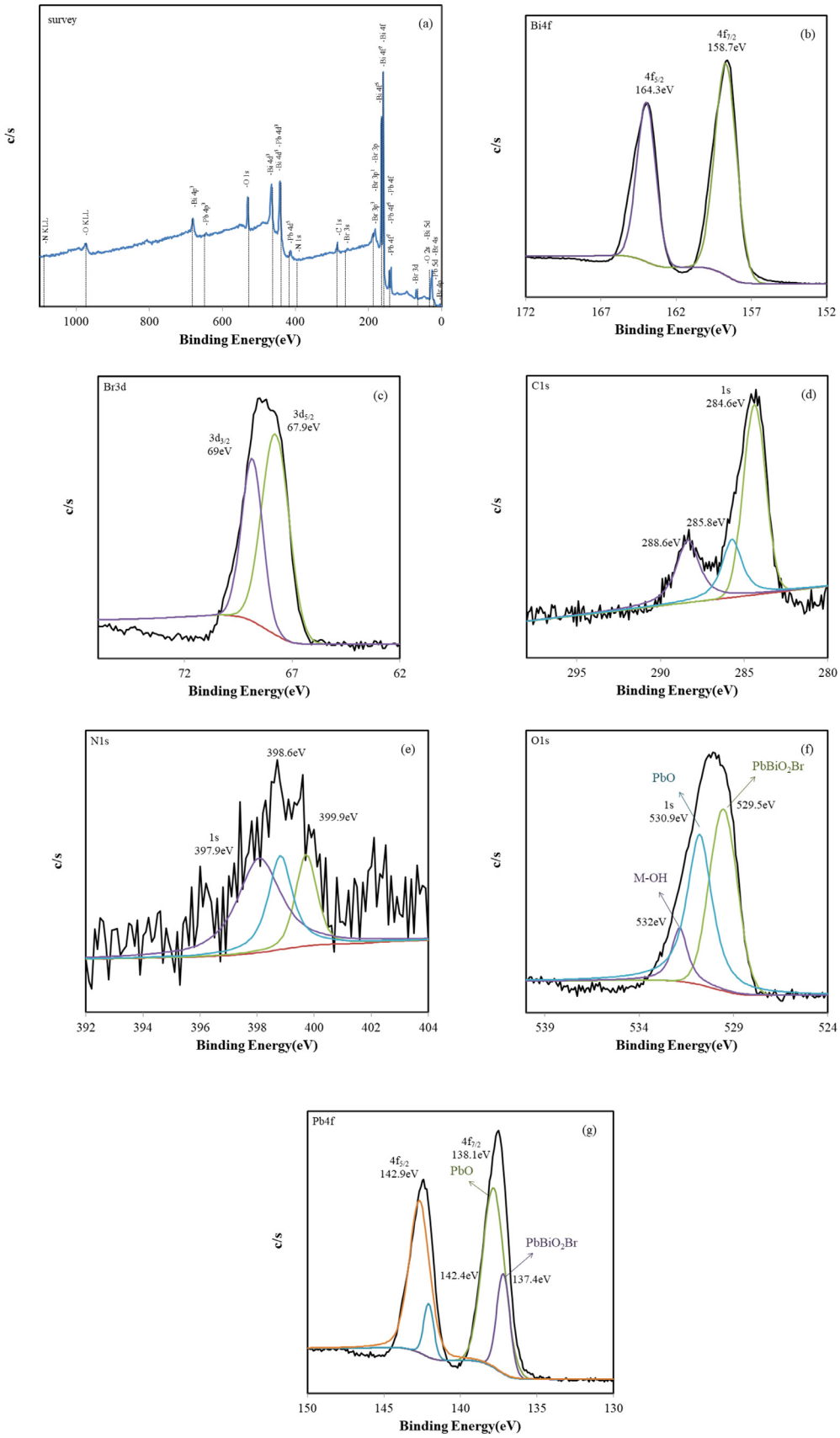

Fig. 5. XPS spectra of as-prepared $PbBiO_2Br/PbO/g\text{-}C_3N_4$ sample. (a) survey of the sample; (b) Bi 4f; (c) Br 3d; (d) C 1 s; (e) N 1 s; (f) O 1 s; (g) Pb 4f.

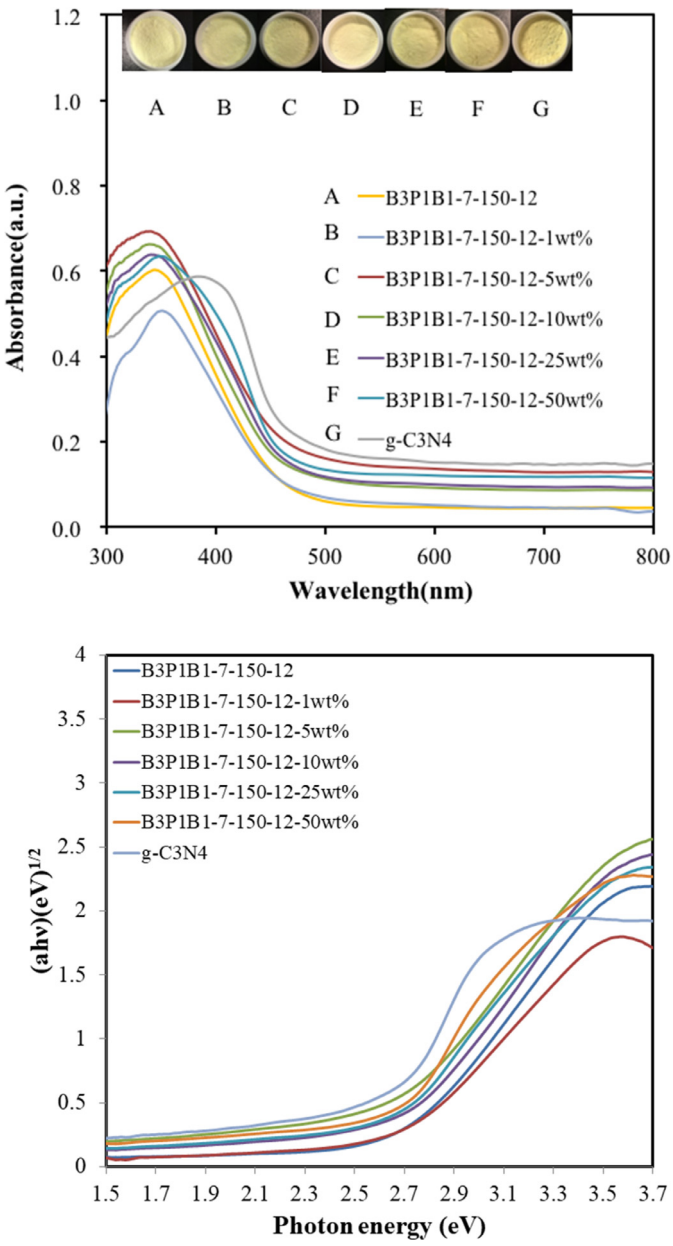

Fig. 6. UV–vis absorption spectra of the as-prepared photocatalysts with various levels of g-C3N4. (Molar ratio $Bi(NO_3)_3/Pb(NO_3)_2 = 3/1$, pH = 7, reaction temp = 150 °C, reaction time = 12 h).

$Pb(OH)_2 \rightarrow PbO \rightarrow Pb_2O_3$. Controlling the hydrothermal reaction's pH yielded various compositions:

$$Bi^{3+} + 3OH^- \rightarrow Bi(OH)_{3(s)} \quad (1)$$

$$Bi(OH)_{3(s)} + Br^- \rightarrow BiOBr_{(s)} + H_2O + OH^- \quad (2)$$

$$Bi^{3+} + 3Br^- \rightarrow BiBr_{3\,(s)} \quad (3)$$

$$BiBr_{3\,(s)} + 2OH^- \rightarrow BiOBr_{\,(s)} + 2Br^- + H_2O \quad (4)$$

$$3BiOBr_{(s)} + 2OH^- \rightarrow Bi_3O_4Br_{(s)} + 2Br^- + H_2O \quad (5)$$

$$Pb^{2+} + 2Br^- \rightarrow PbBr_{2\,(s)} \quad (6)$$

$$PbBr_{2\,(s)} + 2OH^- \rightarrow Pb(OH)_2 + 2Br^- \quad (7)$$

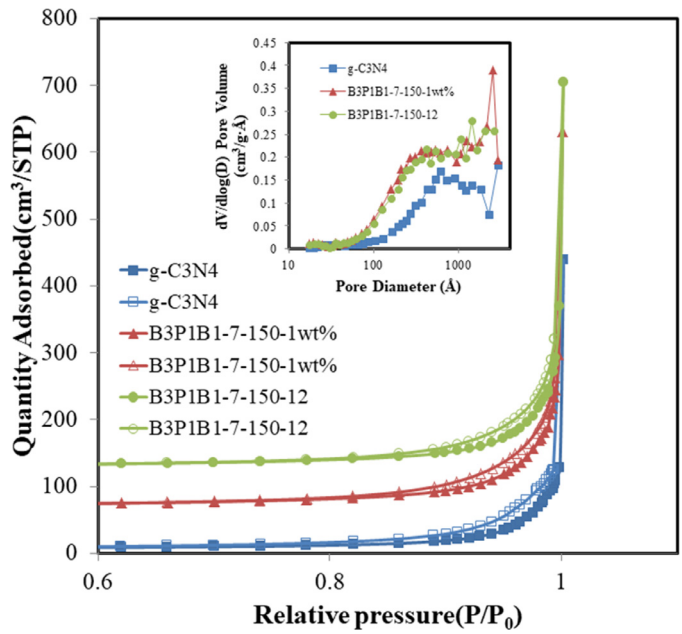

Fig. 7. Nitrogen absorption-desorption isotherms of $PbBiO_2Br/PbO/g\text{-}C_3N_4$ (B3P1B1-7-150-1wt%), $PbBiO_2Br/PbO$(B3P1B1-7-150-12) and $g\text{-}C_3N_4$.

Table 4
Pseudo-first-order rate constant for CV photocatalytic oxidation under different photocatalysts.

	k	R^2
B3P1B1-7-150-12	0.1602	0.9777
B3P1B1-7-150-12-1wt%	**0.1981**	0.9855
B3P1B1-7-150-12-5wt%	0.0713	0.9585
B3P1B1-7-150-12-10wt%	0.1486	0.9854
B3P1B1-7-150-12-25wt%	0.071	0.8692
B3P1B1-7-150-12-50wt%	0.0514	0.9243
B3P1B1-4-150-12	0.1052	0.964
B3P1B1-4-150-12-1wt%	**0.15**	0.9842
B3P1B1-4-150-12-5wt%	0.1097	0.9612
B3P1B1-4-150-12-10wt%	0.0867	0.9745
B3P1B1-4-150-12-25wt%	0.1172	0.9332
B3P1B1-4-150-12-50wt%	0.0784	0.8383
B3P3B1-4-150-12	0.1263	0.9807
B3P3B1-4-150-12-1wt%	**0.1382**	0.818
B3P3B1-4-150-12-5wt%	0.1002	0.9559
B3P3B1-4-150-12-10wt%	0.0688	0.8164
B3P3B1-4-150-12-25wt%	0.0867	0.9069
B3P3B1-4-150-12-50wt%	0.0601	0.9509
B3P3B1-1-100-12	0.1009	0.9783
B3P3B1-1-100-12-1wt%	**0.1726**	0.9637
B3P3B1-1-100-12-5wt%	0.0714	0.9045
B3P3B1-1-100-12-10wt%	0.0773	0.8698
B3P3B1-1-100-12-25wt%	0.0883	0.9123
B3P3B1-1-100-12-50wt%	0.0524	0.8883
B3P5B1-4-150-12	0.152	0.9283
B3P5B1-4-150-12-1wt%	**0.1974**	0.8657
B3P5B1-4-150-12-5wt%	0.1484	0.9433
B3P5B1-4-150-12-10wt%	0.1318	0.9832
B3P5B1-4-150-12-25wt%	0.0951	0.9613
B3P5B1-4-150-12-50wt%	0.0994	0.9208
B3P5B1-1-100-12	0.0392	0.9594
B3P5B1-1-100-12-1wt%	**0.1178**	0.8612
B3P5B1-1-100-12-5wt%	0.1083	0.9009
B3P5B1-1-100-12-10wt%	0.1152	0.8793
B3P5B1-1-100-12-25wt%	0.0681	0.952
B3P5B1-1-100-12-50wt%	0.0545	0.882

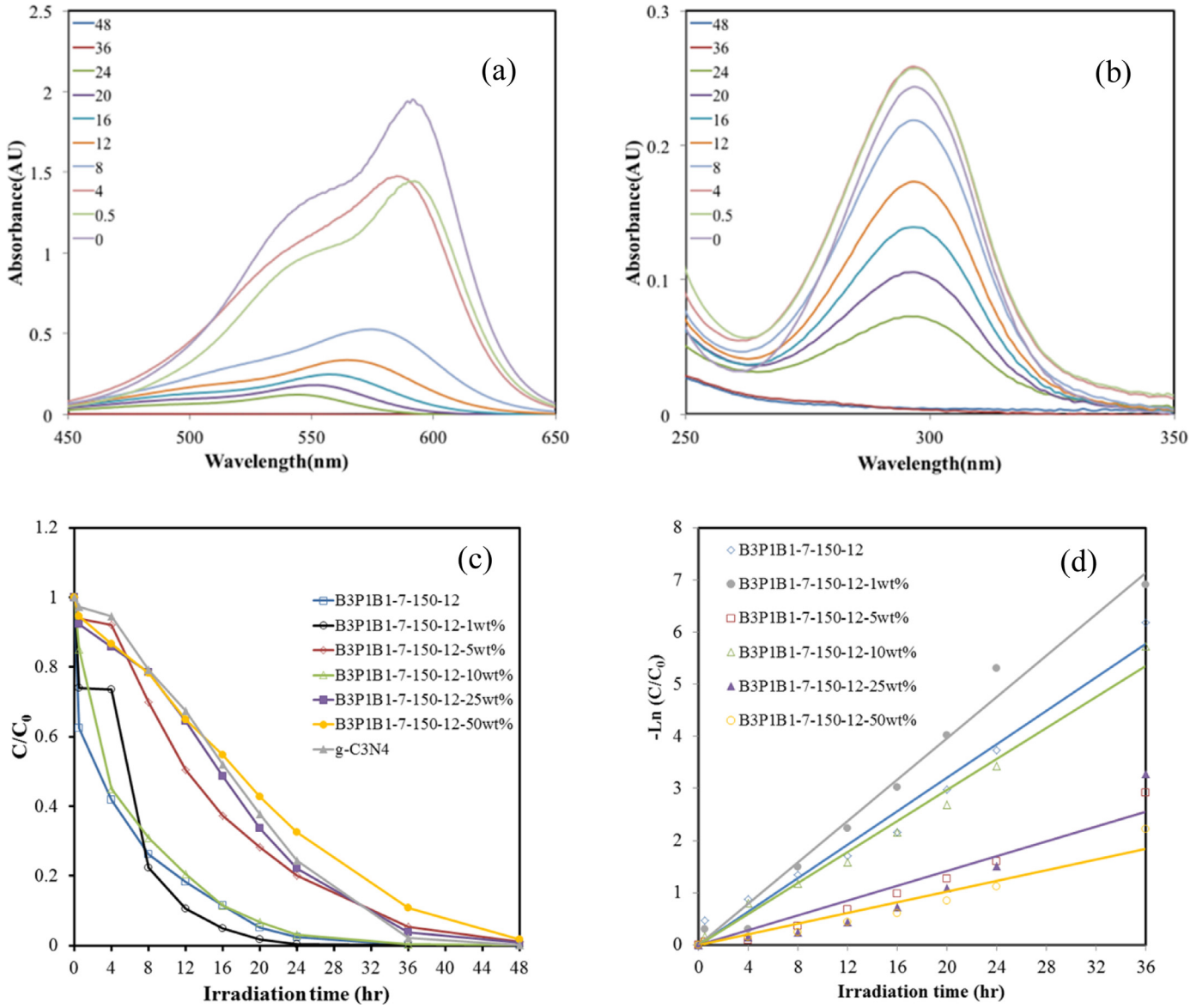

Fig. 8. (a) (b) Temporal UV–vis adsorption spectra of CV and HBA and (c)(d) Photocatalytic degradation of CV as a function of irradiation time over different photocatalysts.

$$BiOBr_{(s)} + Pb(OH)_2 \rightarrow PbBiO_2Br_{(s)} + H_2O \quad (8)$$

$$Pb(OH)_2 \rightarrow PbO_{(s)} + H_2O \quad (9)$$

$$2PbO_{(s)} + H_2O \rightarrow Pb_2O_3 + 2H^+ + 2e^- \quad (10)$$

$$BiOBr_{(s)} + Pb(OH)_2 + g\text{-}C_3N_4 \rightarrow PbBiO_2Br/g\text{-}C_3N_{4\,(s)} + H_2O \quad (11)$$

$$BiOBr_{(s)} + 2Pb(OH)_2 + g\text{-}C_3N_4 \rightarrow PbBiO_2Br/PbO/g\text{-}C_3N_{4\,(s)} + 2H_2O \quad (12)$$

3.1.6. Optical absorption properties

The diffuse-reflectance ultraviolet (UV) results derived for the as-prepared samples revealed the samples' absorption edges to be approximately 430–570 nm (Figs. 6, S5, and S6); these were engendered by the 2.88–2.18-eV band gap; these results conformed with reports in the literature [20,49,50]. Only a modest quantity of visible light is absorbed by pure $PbBiO_2Br/PbO$ and g-C_3N_4. An $(\alpha h\nu)^{1/2}$ plot against energy ($h\nu$) determined the $PbBiO_2Br/PbO/g\text{-}C_3N_4$ E_g value (*i.e.*, 2.53 eV).

3.1.7. Adsorption–desorption isotherm and BET

Fig. 7 illustrates the isotherm curves of N_2 adsorption–desorption derived for $PbBiO_2Br/PbO/g\text{-}C_3N_4$, $PbBiO_2Br/PbO$, and g-C_3N_4. The $PbBiO_2Br/PbO/g\text{-}C_3N_4$ isotherm was noted to approximate Type IV isotherms along with a hysteresis loop observed at a relatively high pressure of 0.6–1.0 [51]. Because such types of self-organized porous architectures afford highly efficient pathways for the reactant and product molecule transport, they are remarkably valuable in photocatalysis [52]. The $PbBiO_2Br/PbO/g\text{-}C_3N_4$, $PbBiO_2Br/PbO$, and g-C_3N_4 samples had S_{BET} values of 31.57, 0.30, and 18.44 $m^2\ g^{-1}$. The pore volume and diameter of $PbBiO_2Br/PbO/g\text{-}C_3N_4$ were 0.285 $cm^3\ g^{-1}$ and 304.2 nm, respectively.

3.2. Photocatalytic activity

Visible light irradiation produced CV and HBA photodegradation in the aqueous $PbBiO_2Br/PbO/g\text{-}C_3N_4$ dispersions; that photodegradation caused some variations in the UV–visible spectra, as depicted in Fig. 8(a), (b). After 48 h of irradiation, approximately 99.9% of CV and approximately 99% of HBA suffered degradation.

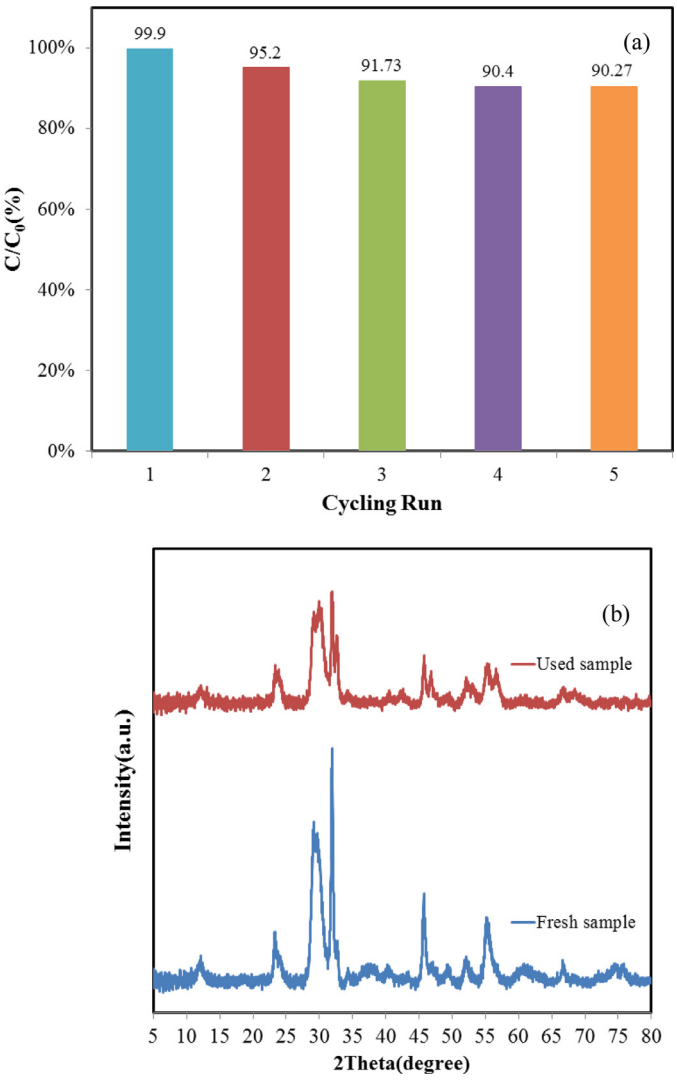

Fig. 9. (a) Cycling runs and (b) XRD patterns acquired before and after in the photocatalytic degradation of CV in the presence of B3P1B1-7-150-1wt% ($PbBiO_2Br/PbO/g\text{-}C_3N_4$).

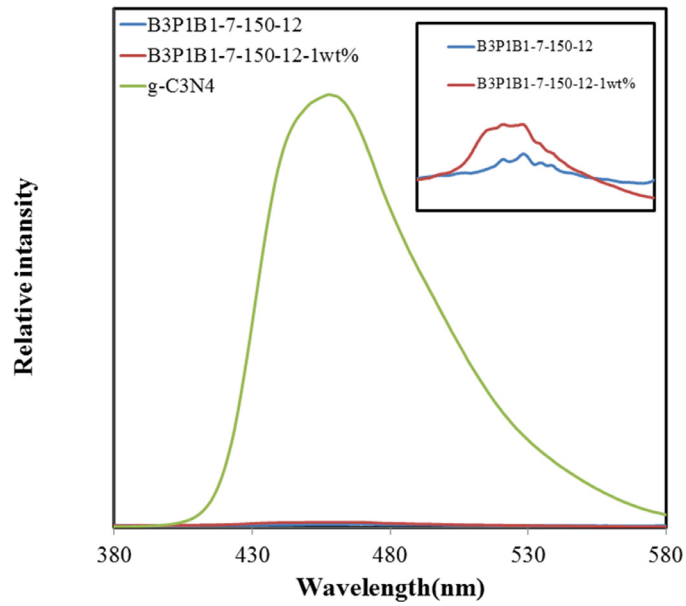

Fig. 10. Photoluminescence (PL) spectra of the $PbBiO_2Br/PbO/g\text{-}C_3N_4$ (B3P1B1-7-150-1wt%), $PbBiO_2Br/PbO$(B3P1B1-7-150-12) and $g\text{-}C_3N_4$.

At approximately 588 nm we observed a typical CV dye absorption band. Visible light irradiation altered the dye, diminished the band rapidly, and produced slight hypsochromic shifts (550 nm); no other absorption band was observed; no band appeared in the UV range ($\lambda > 200$ nm). It would seem that a sequence of *N*-de-methylated intermediates had formed; it is possible that the CV dye's conjugated chromophore structure split. Still more irradiation diminished the absorption band at 550 nm, but did not produce any additional shift in wavelength; therefore, we consider that the 550-nm absorption band corresponded to the full *N*-de-methylated product of the applied CV dye [37,42].

Figs. 8(c),(d), S7, and S8 plot derived degradation efficiency as a function of reaction time. The as-prepared samples exhibited noteworthy efficiency effects. Irradiation for 24 h eliminated as much as 99% of the CV dye and raised the photocatalytic performance level of $PbBiO_2Br/PbO/g\text{-}C_3N_4$ beyond the levels of the other samples. In the context of the degradation reaction kinetics, an apparent pseudo-first-order model [48,53], namely $\ln(C_o/C) = kt$, was calculated. As presented in Table 4, the data demonstrated a first-order linear fit; the maximum degradation rate k of $PbBiO_2Br/PbO/g\text{-}C_3N_4$ was 1.981×10^{-1} h^{-1}, but the k values of the other composites were lower. The order of rate constant presents $PbBiO_2Br/PbO/g\text{-}C_3N_4$, $k = 0.1981 > PbBiO_2Br/PbO$, $k = 0.1602 > PbBiO_2Br$, $k = 0.1235 > PbO$, $k = 0.017$. The maximal effectiveness was displayed by the $PbBiO_2Br/PbO/g\text{-}C_3N_4$ photocatalyst. Catalyst was used, centrifuged, collected, and recycled for additional use so that the durability the $PbBiO_2Br/PbO/g\text{-}C_3N_4$ composite could be evaluated. After four cycles, the CV was eliminated, but no deficit in photocatalytic activity was observed; Fig. 9(a) displays a 9.6% deficit in the fifth run. XRD was applied to samples of used $PbBiO_2Br/PbO/g\text{-}C_3N_4$ but the results given in Fig. 9(b) revealed no difference between the used sample and an as-prepared sample; therefore the photostability of $PbBiO_2Br/PbO/g\text{-}C_3N_4$ composite was noteworthy.

The composites had augmented photocatalytic activity. One might attribute the augmentation to heterojunction formation or to synergistic elements, including a low-energy band structure, a layered structure, and a large BET surface area. Regarding the heterostructures, the $PbBiO_2Br/PbO/g\text{-}C_3N_4$ composites had a small BET surface area, which would suggest relatively low photocatalytic activity. One might expect that the photonic excitation of applied photocatalysts would generate electron–hole pairs immediately. The rate of recombination of electron–hole pairs drives the efficiency of photocatalytic processes. The faster the rate of recombination is, the shorter the chemical reaction time is. Photoluminescence (PL) spectra can provide relevant information regarding photogenerated carrier segregation capacity in heterostructures; Fig. 10 illustrates $PbBiO_2Br/PbO/g\text{-}C_3N_4$ PL spectra. The as-prepared samples exhibited a strong emission peak at approximately 460 nm, caused by the band transitions' direct electron–hole recombination. At the lowest intensity, the innate emission peak of $PbBiO_2Br/PbO/g\text{-}C_3N_4$ was at approximately 460 nm; this was caused by noteworthy inhibition of photogenerated charge carrier recombination. Efficient segregation of charge extends charge carrier lifetime and promotes the transfer efficiency of interfacial charge to the adsorbed substrates, and thus promotes photocatalytic activity. The observed photocatalytic activity of $PbBiO_2Br/PbO/g\text{-}C_3N_4$ heterojunctions reached the maximum rate constant, namely 0.198 h^{-1}, outperforming $PbBiO_2Br$, PbO, $g\text{-}C_3N_4$, and $PbBiO_2Br/PbO$ by 1.23, 34.2, 4.3, and 1.2 times, respectively. It seems that $PbBiO_2Br/PbO/g\text{-}C_3N_4$ heterojunctions are integral to photocatalytic activity augmentation. The PL findings

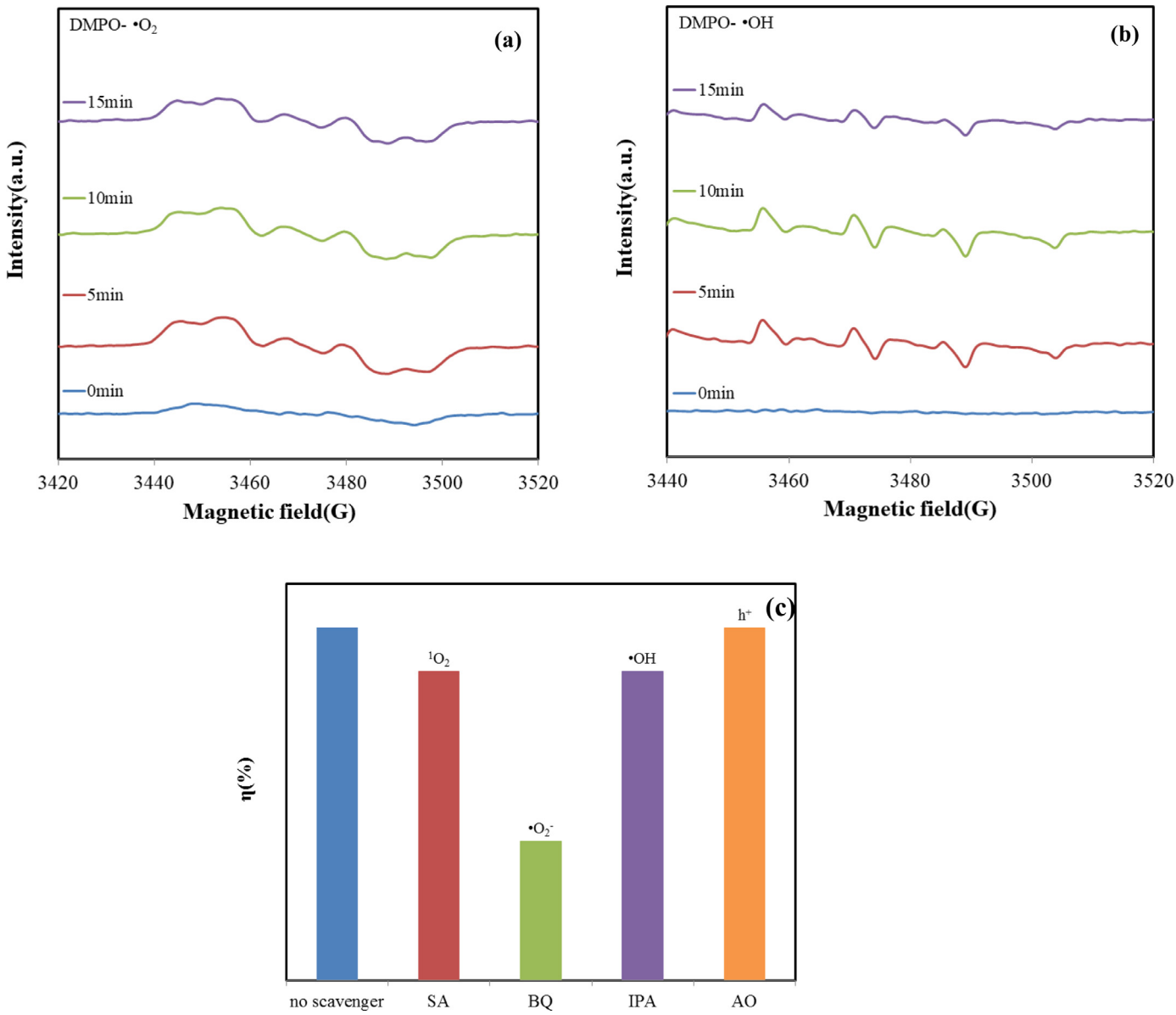

Fig. 11. DMPO spin-trapping EPR spectra for (a) DMPO -$^{\bullet}O_2^-$; (b) DMPO-$^{\bullet}$OH under visible light irradiation with B3P1B1-7-150-1wt%.; (c) Photodegradation of CV dye (B3P1B1-7-150-1wt%) in the presence of different scavengers under solar light irradiation.

explain how the composites obstruct electron–hole recombination and how the $PbBiO_2Br/PbO/g\text{-}C_3N_4$ composites excel at photocatalysis.

3.3. CV photodegradation mechanism

Photocatalytic degradation processes in UV–vis/semiconductor systems can produce diverse primary active species such as HO$^{\bullet}$, h^+, $O_2^{-\bullet}$, H$^{\bullet}$, and $^1O_2$ [54]. In order to evaluate the effect of the active species during the photocatalytic reaction, EPR measurement is used for scavenging the relevant active species. From Fig. 11, only are the characteristic peaks of DMPO–$O_2^{-\bullet}$ and DMPO–OH$^{\bullet}$ adducts observed under visible light irradiated $PbBiO_2Br/PbO/g\text{-}C_3N_4$ suspension. Fig. 11(b) shows that DMPO–OH$^{\bullet}$ EPR signal is observed and Fig. 11(a) shows that weak EPR signals ($^1O_2$) are observed when the reaction is performed in the dark, while the signals with the intensity corresponding to the characteristic peak of DMPO–$O_2^{-\bullet}$ adducts [5,55-57] are observed during the reaction process under visible light irradiation, and the intensity gradually increases with the prolonged reaction time. It suggests that $O_2^{\bullet-}$, $^{\bullet}$OH, and $^1O_2$ being active species are formed in the presence of $PbBiO_2Br/PbO/g\text{-}C_3N_4$ and oxygen under visible light irradiation.

In order to re-evaluate the effect of the active species during the photocatalytic reaction, four quenchers are used for scavenging the relevant active species. As shown in Fig. 11(c), the photocatalytic degradation of CV is obviously affected by the addition of SA, AO, and BQ, and IPA quenching decreases evidently compared with that of no-quenching, indicating that $O_2^{\bullet-}$, $^1O_2$, and $^{\bullet}$OH are the active species in the mechanism of photocatalytic degradation of CV. Hence, the quenching effects of scavengers and EPR illustrate that the reactives $O_2^{\bullet-}$play the major role and, $^{\bullet}$OH and $^1O_2$ play the minor role in the photocatalytic degradation of CV. The generation of $O_2^{-\bullet}$ could not only inhibit the recombination of photoinduced charge carriers but also benefit the degradation of CV. The $O_2^{-\bullet}$ radical might be formatted by an e^- with O_2 and/or $^1O_2$ with e^-species. The $^1O_2$ might be formatted by an h^+ with $O_2^{-\bullet}$ species. The $^{\bullet}$OH radical might be formatted by an h^+ with H_2O

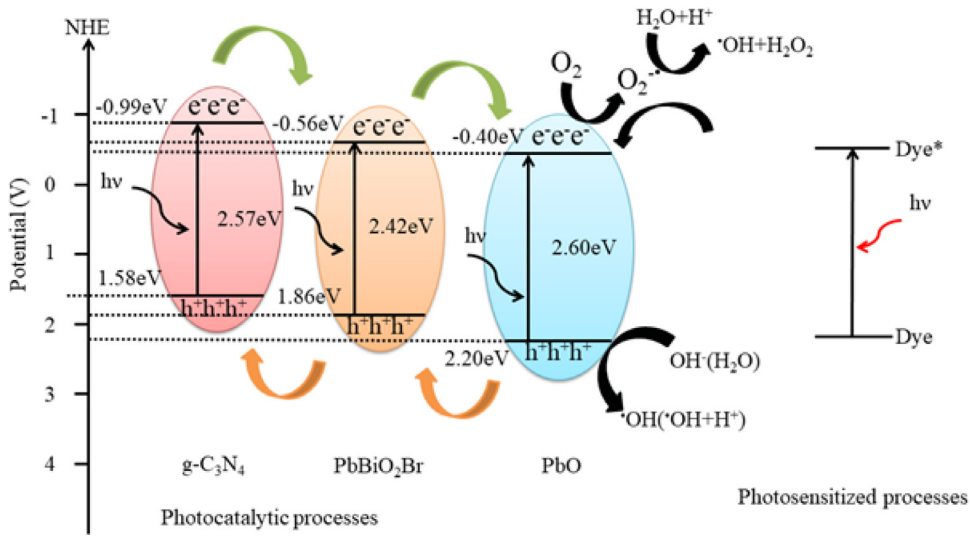

Fig. 12. Band structure diagram of $PbBiO_2Br/PbO/g\text{-}C_3N_4$ and the possible charge separation processes.

and/or $OH^-$with h^+species. Thus, $O_2^{\bullet-}$ could serve as the most crucial active species in this study.

The fact that the $PbBiO_2Br/PbO/g\text{-}C_3N_4$ photocatalyst was a three-phase composite was evident from structural characterizations. Because the derived composite was more active than was the component phase, one might postulate synergistic effects between $PbBiO_2Br/PbO$ and $g\text{-}C_3N_4$. Scholars have reported synergistic effects when two semiconductors are in contact [58,59], and have ascribed such phenomena to efficient transfer of charge across the semiconductor interface; the photoexcited electron–hole segregation and the photocatalytic activity in such experiments have been notably high. An appropriate band potential promotes charge transfer and is necessary for composite photocatalyst synergetic effects. The valance band edge potential (E_{VB}) of $PbBiO_2Br$, PbO, and $g\text{-}C_3N_4$ are 1.86, 2.20 and 1.58 eV, respectively. The band gap (E_g) of $PbBiO_2Br$, PbO, and $g\text{-}C_3N_4$ are 2.42, 2.60 and 2.57 eV, respectively. The E_{VB} of the $PbBiO_2Br$, PbO, and $g\text{-}C_3N_4$ can be calculated by the formula $E_g = E_{VB} - E_{CB}$. Therefore, the conduction band energy (E_{CB}) of $PbBiO_2Br$, PbO, and $g\text{-}C_3N_4$ are −0.56, −0.40 and −0.99 eV, respectively. The results obtained by our calculation are in good agreement with the results reported by previous literatures [11,25,29]. Fig. 12 illustrates heterostructural band alignment derived for a type-II heterostructure [60] and the VB and CB of $PbBiO_2Br$, PbO, and $g\text{-}C_3N_4$. The CB and VB steps are aligned in the same direction, and their positions for the $g\text{-}C_3N_4$ semiconductor are higher than those for the $PbBiO_2Br$ and PbO semiconductors (Fig. 12). As one might have expected from Li et al. [60] $g\text{-}C_3N_4$ had a VB edge at approximately 1.58 eV. The VB edges for $PbBiO_2Br$ and PbO were at 1.86 and 2.20 eV. These results indicate suitable band potentials for $PbBiO_2Br$, PbO, and $g\text{-}C_3N_4$. Light can strike the surface of a $g\text{-}C_3N_4$ sample and produce electrons, which can move to $PbBiO_2Br$ and then to PbO; all of these movements would go through interfaces; the holes in the surface of a PbO sample would move to $PbBiO_2Br$ and then to $g\text{-}C_3N_4$. Thus, our charge transfer obstructed electron–hole recombination in these three semiconductors, and thus boosted photocatalytic efficiency.

Fig. 12 illustrates dye degradation, as known from experimental evidence. After an electron moves to the $PbBiO_2Br/PbO/g\text{-}C_3N_4$ conduction band, that electron triggers the creation of active oxygen species, leading to the degradation of CV dye. Even though CV dye photodegradation enacted by $PbBiO_2Br/PbO/g\text{-}C_3N_4$-mediated and photosensitized processes is crucial, but the boosting of photocatalytic activity must not be ignored. Photosensitized and photocatalytic processes occur simultaneously (Fig. 12). In photosensitized and photocatalytic reactions, photogenerated and photosensitized electrons react with oxygen on the surface of a photocatalyst, and produce $O_2^{\bullet-}$ radicals; those $O_2^{\bullet-}$radicals react with H^+ ions; h^+ holes react with OH^- ions (or H_2O) to produce $^{\bullet}OH$ radicals. After electrons produce $O_2^{\bullet-}$ radicals, those $O_2^{\bullet-}$radicals react with H^+ ions. $^1O_2$ reacts with electrons, and h^+ holes react with OH^- ions (or H_2O) to generate $^{\bullet}OH$ radicals. Visible light causes these cycles to persist [61]; when numerous photooxidation cycles have run their course, Eqs. (13) and (14) elucidate the CV dye degradation.

$$CV + O_2^{-\bullet}/^{\bullet}OH \rightarrow \text{degraded compounds} \quad (13)$$

$$CV^{+\bullet} + O_2^{-\bullet}/^{\bullet}OH \rightarrow \text{degraded compounds} \quad (14)$$

A study of a semiconductor system galvanized by visible light described hydroxylated compounds for photocatalytic CV dye degradation [61]. Published reports [32,37,51] have proven that *N*-centered radical production goes before *N*-de-alkylation; furthermore, carbon-centered radical production goes before dye chromophore structure demolition when ultraviolet or visible light degrades CV dye. Our present findings regarding $PbBiO_2Br/PbO/g\text{-}C_3N_4$ photocatalysis can be useful for various dye-decoloration applications.

4. Conclusions

For the first time, $PbBiO_2Br/PbO/g\text{-}C_3N_4$ heterojunctions were synthesized hydrothermally and without templates. The use of $PbBiO_2Br/PbO/g\text{-}C_3N_4$ significantly improved removal efficiency. We proved that $PbBiO_2Br/PbO/g\text{-}C_3N_4$ photocatalytic activity enhancement corresponded to the formation of heterojunctions between $PbBiO_2Br$, PbO, and $g\text{-}C_3N_4$. Those heterojunctions enhanced $PbBiO_2Br/PbO/g\text{-}C_3N_4$ photocatalytic activity. This phenomenon effectively obstructed the recombination of photogenerated electrons and holes. The observed photocatalytic degradation of CV dye was largely caused by reactive $O_2^{\bullet-}$; four scavengers demonstrated quenching effects. The methods explained in this paper are useful for $PbBiO_2Br/PbO/g\text{-}C_3N_4$ synthesis and CV dye photocatalytic degradation. These methods can be applied to rectify environmental pollution.

Acknowledgments

This research was supported by the Ministry of Science and Technology of the Republic of China (MOST-106-2113-M-142-001). We acknowledge Wallace Academic Editing for editing this manuscript.

Supplementary materials

Supplementary material associated with this article can be found, in the online version, at doi:10.1016/j.jtice.2018.07.037.

References

[1] Hoffmann MR, Martin ST, Choi W, Bahnemann DW. Environmental applications of semiconductor photocatalysis. Chem Rev 1995;95:69–96.
[2] Kubacka A, Fernández-García M, Colón G. Advanced Nanoarchitectures for solar photocatalytic applications. Chem Rev 2012;112:1555–614.
[3] Huang ST, Jiang YR, Chou SY, Dai YM, Chen CC. Synthesis, characterization, photocatalytic activity of visible-light-responsive photocatalysts BiO_xCl_y/BiO_mBr_n by controlled hydrothermal method. J Mol Catal A: Chem 2014;391:105–20.
[4] Cheng H, Huang B, Dai Y. Engineering BiOX (X = Cl, Br, I) nanostructures for highly efficient photocatalytic applications. Nanoscale 2014;6:2009–26.
[5] Huang H, Han X, Li X, Wang S, Chu PK, Zhang Y. Fabrication of multiple heterojunctions with tunable visible-light-active photocatalytic reactivity in BiOBr–BiOI full-range composites based on microstructure modulation and band structures. ACS Appl Mater Interfaces 2015;7:482–92.
[6] Huang H, Xiao K, He Y, Zhang T, Zhang Y. In situ assembly of $BiOI@Bi_{12}O_{17}Cl_2$ p-n junction: charge induced unique front-lateral surfaces coupling heterostructure with high exposure of BiOI {001} active facets for robust and nonselective photocatalysis. Appl Catal B: Environ 2016;199:75–86.
[7] Chen Z, Jiang H, Jin W, Shi C. Enhanced photocatalytic performance over $Bi_4Ti_3O_{12}$ nanosheets with controllable size and exposed {001} facets for Rhodamine B degradation. Appl Catal B: Environ 2016;180:698–706.
[8] Seabold JA, Choi KS. Efficient and stable photo-oxidation of water by a bismuth vanadate photoanode coupled with an iron oxyhydroxide oxygen evolution catalyst. J Am Chem Soc 2012;134:2186–92.
[9] Wei W, Dai Y, Huang BB. First-principles characterization of Bi-based photocatalysts: $Bi_{12}TiO_{20}$, $Bi_2Ti_2O_7$, and $Bi_4Ti_3O_{12}$. J Phys Chem: C 2009;113:5658–63.
[10] Batuk M, Batuk D, Tsirlin AA. Filimonov DS. Layered oxychlorides $[PbBiO_2]A_{n+1}BnO_{3n-1}Cl_2$ (A = Pb Bi^{-1}, B = Fe/Ti): intergrowth of the hematophanite and sillen phases. Chem Mater 2015;27:2946–56.
[11] Lin HP, Lee WW, Huang ST, Chen LW, Yeh TW, Fu JY, Chen CC. Controlled hydrothermal synthesis of $PbBiO_2Br$/BiOBr heterojunction with enhanced visible–driven-light photocatalytic activities. J Mol Catal A: Chem 2016;417:168–83.
[12] Yu Y, Gu Y, Zheng W, Ding Y, Cao Y. New type photocatalyst $PbBiO_2Cl$: materials design and experimental validation. J Phys Chem:C 2015;119:28190–3.
[13] Liu FY, Jiang YR, Chen CC, Lee WW. Novel synthesis of $PbBiO_2Cl$/BiOCl nanocomposite with enhanced visible-driven-light photocatalytic activity. Catal Today 2018;300:112–23.
[14] Wang B, Di J, Zhang PF, Xia JX, Dai S, Li HM. Ionic liquid-induced strategy for porous perovskite-like $PbBiO_2Br$ photocatalysts with enhanced photocatalytic activity and mechanism insight. Appl Catal B: Environ 2017;206:127–35.
[15] Yin S, Wu T, Li M, Di J, Ji M, Wang B, Chen Y, Xia J, Li H. Controllable synthesis of perovskite-like $PbBiO_2Cl$ hollow microspheres with enhanced photocatalytic activity for antibiotic removal. CrystEngComm 2017;19:4777–88.
[16] Ketterer J, Krämer V. Structural characterization of the synthetic perites $PbBiO_2X$, X= I, Br, Cl. Mater Res Bull 1985;20:1031–6.
[17] Xiao FY, Xing J, Wu L, Chen ZP, Wang XL, Yang HG. Assembly of ultrathin $PbBiO_2Br$ nanosheets with enhanced visible light photocatalytic properties. RSC Adv 2013;3:10687–90.
[18] Shan Z, Lin X, Liu M, Ding H, Huang F. A Bi-based oxychloride $PbBiO_2Cl$ as a novel efficient photocatalyst. Solid State Sci 2009;11:1163–9.
[19] Rau S, Sch¨afer B, Gleich D, Anders E, Rudolph M, Friedrich M, G¨orls H, Henry W, Vos JG. Ein supramolekularer Photokatalysator zur Erzeugung von Wasserstoff und zur selektiven Hydrierung von Tolan. Angew Chem 2006;118:6361–4.
[20] F¨uldner S, Pohla P, Bartling H, Dankesreiter S, Stadler R, Gruber M, Pfitzner A, K¨onig B. Selective photocatalytic reductions of nitrobenzene derivatives using $PbBiO_2X$ and blue light. Green Chem 2011;13:640–3.
[21] Huang H, Xiao K, Ti Zhang, Dong F, Zhang Y. Rational design on 3D hierarchical bismuth oxyiodides via in situ self-template phase transformation and phase-junction construction for optimizing photocatalysis against diverse contaminants. Appl Catal B: Environ 2017;203:879–88.
[22] Shan Z, Wang W, Lin X, Ding H, Huang F. Photocatalytic degradation of organic dyes on visible-light responsive photocatalyst $PbBiO_2Br$. J Solid State Chem 2008;181:1361–6.
[23] Xiao FY, Xing J, Wu L, Chen ZP, Wang XL, Yang HG. Assembly of ultrathin $PbBiO_2Br$ nanosheets with enhanced visible light photocatalytic properties. RSC Adv 2013;3:10687–90.
[24] Huang H, Tu S, Zeng C, Zhang T, Reshak AH, Zhang Y. Macroscopic polarization enhancement promoting photo- and piezoelectric-induced charge separation and molecular oxygen activation. Angew Chem Int Ed Engl 2017;56:11860–4.
[25] Wang B, Di J, Liu G, Yin S, Xia J, Zhang Q, Li H. Novel mesoporous graphitic carbon nitride modified $PbBiO_2Br$ porous microspheres with enhanced photocatalytic performance. J Colloid Interface Sci 2017;507:310–22.
[26] Li S, Wang X, Xu Y, Yang H, Wei F, Liu X. The excellent photocatalytic synergism of $PbBiO_2Br$/UiO-66-NH_2 composites via multiple coupling effects. RSC Adv 2016;6:89907–15.
[27] Guo H, Niu CG, Wen XJ, Zhang L, Zeng GM. Construction of highly efficient and stable ternary AgBr/Ag/$PbBiO_2Br$ Z-scheme photocatalyst under visible light irradiation: performance and mechanism insight. J Colloid Interface Sci 2018;513:852–65.
[28] Li X, Wang J, Xu D, Sun Z, Zhao Q, Peng W, Li Y, Zhang G, Zhang F, Fan X. $NbSe_2$ nanosheet supported $PbBiO_2Br$ as a high performance photocatalyst for the visible light-driven asymmetric alkylation of aldehyde. ACS Sustainable Chem Eng 2015;3:1017–22.
[29] Liu FY, Lin JH, Dai YM, Chen CC. Preparation of perovskites $PbBiO_2I$/PbO exhibiting visible-light photocatalytic activity. Catal Today 2018;314:28–41.
[30] Li M, Yin S, Wu T, Di J, Ji M, Wang B, Chen Y, Xia J, Li H. Controlled preparation of $MoS_2/PbBiO_2I$ hybrid microspheres with enhanced visible-light photocatalytic behavior. J Colloid Interface Sci 2018;517:278–87.
[31] Wang P, Huang B, Qin X, Zhang X, Dai Y, Wei J, Whangbo MH. Ag@AgCl: a highly efficient and stable photocatalyst active under visible light. Angew Chem Int Ed 2008;47:7931–3.
[32] Jiang YR, Lin HP, Chung WH, Dai YM, Lin WY, Chen CC. Controlled hydrothermal synthesis of BiO_xCl_y/BiO_mI_n composites exhibiting visible-light photocatalytic degradation of crystal violet. J Hazard Mater 2015;283:787–805.
[33] Zhang LS, Wong KH, Yip HY, Hu C, Yu JC, Chan CY, Wong PK. Effective photocatalytic disinfection of E. coli K-12 Using AgBr−Ag−Bi_2WO_6 nanojunction system irradiated by visible light: the role of diffusing hydroxyl radicals. Environ Sci Technol 2010;44:1392–8.
[34] Yin MC, Li ZS, Kou JH, Zou ZG. Mechanism investigation of visible light-induced degradation in a heterogeneous TiO_2/Eosin Y/Rhodamine B system. Environ Sci Technol 2009;43:8361–6.
[35] Meng SG, Li DZ, Sun M, Li WJ, Wang JX, Chen J, Fu XZ, Xiao GC. Sonochemical synthesis, characterization and photocatalytic properties of a novel cube-shaped $CaSn(OH)_6$. Catal Commun 2011;12:972–5.
[36] Li G, Wong KH, Zhang X, Hu C, Yu JC, Chan RCY, Wong PK. Degradation of acid orange 7 using magnetic AgBr under visible light: the roles of oxidizing species. Chemosphere 2009;76:1185–91.
[37] Jiang YR, Chou SY, Chang JL, Huang ST, Lin HP, Chen CC. Hydrothermal synthesis of bismuth oxybromide-bismuth oxyiodide composites with highly visible light photocatalytic performance for the degradation of CV and phenol. RSC Adv 2015;5:30851–60.
[38] Chou SY, Chung WH, Chen LW, Dai YM, Lin WY, Lin JH, Chen CC. A series of BiO_xI_y/GO photocatalysts: synthesis, characterization, activity, and mechanism. RSC Adv 2016;6:82743–58.
[39] Yan SC, Li ZS, Zou ZG. Photodegradation performance of g-C_3N_4 fabricated by directly heating melamine. Langmuir 2009;25:10397–401.
[40] Huang H, Xiao K, Tian N, Dong F, Zhang T, Du X, Zhang Y. Template-free precursor-surface-etching route to porous, thin g-C_3N_4 nanosheets for enhancing photocatalytic reduction and oxidation activity. J Mater Chem A 2017;5:17452–63.
[41] Zhang J, Zhang M, Zhang Wang X. Synthesis of carbon nitride semiconductors in sulfur flux for waterphotoredox catalysis. ACS Catal 2012;2:940–8.
[42] Chen HL, Lee WW, Chung WH, Lin HP, Chen YJ, Jiang YR, Lin WY, Chen CC. Controlled hydrothermal synthesis of bismuth oxybromides and their photocatalytic properties. J Taiwan Inst Chem Eng 2014;45:1892–909.
[43] Li Y, Zhang H, Liu P, Wang D, Li Y, Zhao H. Cross-linked g-C_3N_4/rGO nanocomposites with tunable band structure and enhanced visible light photocatalytic activity. Small 2013;9:3336–44.
[44] Zhang J, Zhang M, Zhang G, Wang X. Harnessing protein symmetry for enzyme design. ACS Catal 2012;2:940–8.
[45] Rahman MM, Krishna KM, Soga T, Jimbo T, Umeno M. Optical properties and X-ray photoelectron spectroscopic study of pure and Pb-doped TiO_2 thin films. J Phys Chem Solid 1999;60:201–10.
[46] Li M, Yin S, Wu T, Di J, Li H. Controlled preparation of $MoS_2/PbBiO_2I$ hybrid microspheres with enhanced visible-light photocatalytic behavior. J Colloid Interface Sci 2018;517:278–87.
[47] Jiang YR, Chou SY, Chang JL, Huang ST, Lin HP, Chen CC. Hydrothermal synthesis of bismuth oxybromide-bismuth oxyiodide composites with highly visible light photocatalytic performance for the degradation of CV and phenol. RSC Adv 2015;5:30851–60.
[48] Pfitzner A, Pohla P. Syntheses and crystal structures of $PbSbO_2Br$, $PbSbO_2I$, and $PbBiO_2Br$. J Inorg General Chem 2009;635:1157–9.
[49] Barbero BP, Cadus LE. V_2O_5–$SmVO_4$ mechanical mixture: oxidative dehydrogenation of propane. Appl Catal: A 2002;237:263–73.
[50] Lee WW, Lu CS, Chuang CW, Chen YJ, Fu JY, Siao CW, Chen CC. Synthesis of bismuth oxyiodides and their composites: characterization, photocatalytic activity, and degradation mechanisms. RSC Adv 2015;5:23450–63.
[51] Fan HJ, Lu CS, Lee WLW, Chiou MR, Chen CC. Mechanistic pathways differences between P25-TiO_2 and Pt-TiO_2 mediated CV photodegradation. J Hazard Mater 2011;185:227–35.
[52] Dong F, Sun Y, Fu M, Wu Z, Lee SC. Room temperature synthesis and highly

enhanced visible light photocatalytic activity of porous BiOI/BiOCl composites nanoplates microflowers. J Hazard Mater 2012;219–220:26–34.
[53] Chatzitakis A, Berberidou C, Paspaltsis I, Kyriakou G, Sklaviadis T, Poulios I. Photocatalytic degradation and drug activity reduction of chloramphenicol. Water Res 2008;42:386–94.
[54] Dimitrijevic NM, Vijayan BK, Poluektov OG, Rajh T, Gray KA, He H, Zapol P. Role of water and carbonates in photocatalytic transformation of CO_2 to CH_4 on titania. J Am Chem Soc 2011;133:3964–71.
[55] Huang Hongwei, Li Xiaowei, Wang Jinjian, Dong Fan, Chu Paul K, Zhang Tierui, Zhang Yihe. Anionic group self-doping as a promising strategy: band-gap engineering and multi-functional applications of high-performance CO_3^{2-}-Doped $Bi_2O_2CO_3$. ACS Catal 2015;5:4094–103.
[56] Huang H, He Y, Li X, Li M, Zeng C, Dong F, Du X, Zhang T, Zhang Y. $Bi_2O_2(OH)(NO_3)$ as a desirable $[Bi_2O_2]^{2+}$ layered photocatalyst: strong intrinsic polarity, rational band structure and {001} active facets co-beneficial for robust photooxidation capability. J Mater Chem A 2015;3:24547–56.
[57] Xiao X, Xing C, He G, Zuo X, Nan J, Wang L. Solvothermal synthesis of novel hierarchical $Bi_4O_5I_2$ nanoflakes with highly visible light photocatalytic performance for the degradation of 4-tert-butylphenol. Appl Catal B: Environ 2014;148–149:154–63.
[58] Li H, Zhou Y, Tu W, Ye J, Zou Z. State-of-the-Art progress in diverse heterostructured photocatalysts toward promoting photocatalytic performance. Adv Funct Mater 2015;25:998–1013.
[59] Li Z, Feng J, Yan S, Zou Z. Solar fuel production: Strategies and new opportunities with nanostructures. Nano Today 2015;10:468–86.
[60] Falcoń H, Barbero JA, Alonso JA, Martıńez-Lope MJ, Fierro JLG. $SrFeO_{3-\delta}$ perovskite oxides: chemical features and performance for methane combustion. Chem Mater 2002;14:2325–33.
[61] Tian Y, Chang B, Lu J, Fu J, Xi F, Dong X. Hydrothermal synthesis of graphitic carbon nitride–Bi_2WO_6 heterojunctions with enhanced visible light photocatalytic activities. ACS Appl Mater Interface 2013;5:7079–85.